



Predictive microstructure image generation using denoising diffusion probabilistic models

Erfan Azqadan^{*}, Hamid Jaled, Arash Arami

Department of Mechanical and Mechatronics Engineering, University of Waterloo, 200 University Ave W, Waterloo, ON N2L 3G1, Canada



ARTICLE INFO

Keywords:
 Denoising diffusion probabilistic model
 Magnesium alloys
 Cast-forging
 Image generation
 $Mg_{17}Al_{12}$ intermetallic
 Dynamic recrystallization

ABSTRACT

The rapid progress in artificial intelligence (AI) based image generation led to groundbreaking achievements, like OpenAI's DALL-E 2, showcasing state-of-the-art generative models in deep learning and computer vision. Recently, the Denoising Diffusion Probabilistic Model (DDPM) has emerged as a strong contender, excelling in generating high-resolution images with complex features similar to those found in real-world images. In this study, we investigate DDPM's potential as both generator and predictor of scanning electron microscope (SEM) images, encompassing both known and unseen microstructural conditions. To rigorously evaluate DDPM, we curated a comprehensive dataset comprising 27 distinct cast-forged AZ80 magnesium alloy components with varied process parameters and microstructure features. Some conditions were held back during training to test DDPM's predictive abilities for unseen scenarios. Our study demonstrates the model's remarkable capacity to capture the inherent physical relationships between process parameters and microstructure features. We scrutinize the synthesized images alongside real-world SEM counterparts, undertaking a comprehensive analysis of various morphological properties. Remarkably, the results show the model's performance, with an average error of $6.36\% \pm 0.42$ for measured microstructural properties in seen conditions and an equally impressive $6.67\% \pm 0.85$ for unseen conditions. This study envisions a transformative shift in materials science, as advanced AI predictive models offer new potential to streamline the laborious process of microstructure image generation.

1. Introduction

By virtue of the recent advancements in deep learning models, new tools are introduced to scientific communities that can accelerate research and analysis. Diffusion models are one of the emerging machine learning (ML) models in computer vision, based on the idea of gradually destroying structure in a data distribution with a forward process and restoring structure in data using a tractable model in a backward process, assuming it has learned the underlying data distribution to generate new data [1]. Open AI's text-to-image DALL-E 2 [2] and Microsoft's Bing Image Creator are based on this idea, which was originally inspired by non-equilibrium statistical physics [1]. What has captivated material scientists amidst this advancement is the question of whether this modeling approach can effectively learn underlying physical relationships and subsequently be applied in an informed search for novel materials with desired properties [3,4].

Materials science and engineering has adapted ML methods in material design, characterization, and properties prediction for quite some time [5–7]. Traditionally, the modeling of materials microstructure has

relied on physics-based methods, such as finite element analysis or phase field modeling, which are computationally expensive and require using known physical relationships and constitutive equations [8–10]. When dealing with complex materials, all physical relationships might not be available or incorporation of all of them in a modeling method might make it impossible to find a solution for the analysis. Another challenge in microstructure generation using physics-based methods comes from the multiscale nature of microstructure. While inclusion of atomistic material phenomena in models such as molecular dynamic allows an accurate representation of atomistic interactions, their limited time and length scale prevents capturing of large-scale material behaviors [11, 12]. Recently, the advanced data-driven models are being adapted in materials science to bridge this gap [4,13]. ML generative models have shown success in capturing complex relationships, such as mechanical properties [14] and inverse property to microstructure linkage [15], without the explicit knowledge of the underlying physics, and this capability can be used in relatively fast mesoscale simulation of material's microstructure [16,17]. Nevertheless, beside above ML applications, the microstructure study, as a pivotal aspect of materials science,

* Corresponding author.

E-mail address: eazqadan@uwaterloo.ca (E. Azqadan).

can majorly benefit from ML advancements in the area of computer vision.

In the past few years, many microstructural applications, ranging from microstructure recognition [18] and classification [19,20] to resolution enhancement [21,22], have been expanded by data-driven modeling methods. Nonetheless, the microstructure image generation has remained a less studied aspect due to it being a more technically challenging task. Three major types of ML models have been used to synthesize microstructure images: Generative adversarial network (GAN) [23,24], variational autoencoder (VAE) [25], and most recently denoising diffusion probabilistic models (DDPM) [26,27]. There have been several studies to employ GAN-based models in generating microstructure images [23,24,28,29]. Iyer et al. [23] employed a conditional generative model to synthesize images of an ultra-high carbon steel. They included an auxiliary classifier to help the model account for the influence of processing condition. Moreover, to improve GAN training and mitigate vanishing gradient issue, they replaced the min-max objective by the Wasserstein distance with gradient penalty, known for addressing the issue [30]. With these additional considerations, Iyer et al. were able to generate high quality synthesized microstructure images. To evaluate the similarity of synthesized images to the actual dataset, they have used 2-point spatial correlation and developed an alternative method to extract images features and project them onto a 2-dimensional space for distribution comparison. However, their work is limited to investigating the incorporation of one given process condition. Therefore, it lacks predictive capability for unseen or other process conditions. Lee et al. [29] explored diverse GAN model variations to produce realistic microstructure images of steels, Li-battery cathode, and anode materials. Their study showcased the capabilities and benefits of advanced GAN algorithms using several real-world datasets. However, their study did not include predictive application of the developed models.

Despite significant improvements in performance of GAN-based models [30,31], several dire issues related to the GAN approach, such as mode collapse [32] and unstable training [33], are yet to be solved and have motivated researchers to look for better alternatives. The mode collapse occurs when GAN generator is only able to generate few variations of the input data distribution. Since the introduction of the GAN models, the mode collapse problem has been systematically studied and documented in computer science [32,34]. This issue becomes a more serious problem in application of ML generative models in applied sciences because in these applications certain descriptors are extracted from images. Therefore, producing a limited variety of images results in inaccurate measurement of the descriptors. In materials science, the mode collapse limits the model capability to imitate the physical relationships that exist between parameters and microstructure images. While VAEs are not susceptible to the mode collapse problem due to their probabilistic nature, they tend to generate blurry and less-detailed outputs compared to the input data [35,36]. This is attributed to the modeling of high-dimensional data space to a lower-dimensional latent space in this process [37]. Microstructure images generally contain fine features, such as grain boundaries or second-phase particles, that are only a few pixels in size. The lossy compression nature of VAEs and their lack of fine details results in loss of such vital information in microstructure generation applications.

The emergence of DDPM, a class of diffusion models introduced in 2020 in the field of computer vision, and its application as an alternative method to GAN and VAE, have transformed the generation of high-quality synthesized images [38]. Given the relatively recent development of this model, there have been only few attempts to utilize DDPM models in generating high-quality microstructure images. Lee and Yun [26] have developed a DDPM model to generate images similar to a dataset comprising several diverse types of microstructures (e.g., polycrystalline alloy, carbonate, ceramics, copolymer, fiber composite, etc.). Utilizing images of size 64×64, the authors successfully produced synthesized images visually resembling the microstructures of the targeted

materials. However, their study lacks exploration of the process-to-microstructure connection. In addition, as they employ a generic type of microstructures, the model's ability to learn underlying data distribution remains unexplored. In another study, Vlassis and Sun [39] incorporated materials properties via embedded feature vectors to condition DDPM model to produce microstructure associated with targeted mechanical behavior. The authors have not used real microstructure images, instead they have used the mechanical MNIST dataset [40], which is a dataset of finite element simulation results of total strain energy corresponding to 28×28 pixels images from the MNIST handwritten digit database [40]. Using DDPM, they produced microstructure images that resemble topology and energy responses of those present in the mechanical MNIST dataset. The absence of real-world microstructure images for training and evaluation of the model makes it inconclusive whether the proposed model can effectively capture physical relationships of manufacturing processes outcomes. More recently, Dürer et al. [27] have applied a DDPM model to a generic microstructure dataset collected from the literature along with an in-house fiber composite dataset, to show the model ability to regenerate high-quality microstructure images from a small dataset size. Similar to the previous two studies, the predictability of the model in generating images from unseen conditions was not explored in their work either. Moreover, the image quality is only assessed via the Fréchet inception distance (FID) score, and no discussion on similarity of morphological features is provided. In general, diffusion-based models are reported to be less prone to unstable training and mode collapse [27,39]. Despite the successful demonstration of the ability of DDPM in generating microstructure images, its applications in predicting the microstructure and the associated information from its corresponding processing parameters remains unexplored.

In the application of ML image generative models in materials science, a significant challenge lies in evaluating synthesized images. Computer vision has proposed various image quality metrics (IQMs), ranging from error-based methods like the mean squared error (L2-norm) to perceptual metrics like FID [41,42], offering great improvements in effectiveness of IQMs over the years. For instance, the FID metric, initially introduced by Heusel et al. [43] in 2017, measures the similarity between the real and generated dataset distributions by assessing activation values of intermediate layers computed by the Inception neural network [44] as a feature extractor. This allows the evaluation of real and generated images in feature space, providing a more representative measure of their similarity and dissimilarity. Nonetheless, it is essential to recognize that these IQMs are primarily designed to cater to human perceptions such as object, face, and scene recognition [42]. In contrast, materials scientists are more concerned with the information conveyed by the microstructure images. Consequently, the use of existing IQMs might not guarantee a robust evaluation of generative models in materials science, as they may not fully capture the nuances of microstructural features essential for material analysis. Thus, a tailored approach may be necessary to ensure an accurate and comprehensive evaluation of generative models in the field of materials science.

Besides the necessity of tailored approaches in evaluation of synthesized images in material science, there are few other requirements for DDPM to be used as a predictive tool in material design and analysis. First and foremost, the model must produce high-resolution images comparable to real SEM microstructure images to exhibit long-range microstructure domains features as well as possible heterogeneities. Additionally, as a mesoscale microstructure model, it should produce images not only for known manufacturing routes but also for untrained conditions. The model's generalizability and convergence to include all possible microstructure variations through an analysis of existing physical relationship is also crucial. To date, such a comprehensive ML image generative model remains unexplored in materials science and engineering.

In this study, we explore the potential of DDPM not merely as a

generator of SEM images depicting known microstructures but also as a predictor of SEM images embodying unseen microstructural conditions. In the absence of a comprehensive framework to evaluate the quality of synthesized images produced by generative models in materials science applications, this study employs a dataset- and application-dependent approach for evaluation. We evaluate the performance of the model in generating images *via* the FID score as well as analysis of the microstructure features and their comparison with the measurements of the actual manufactured samples. To rigorously assess DDPM's ability, we have carefully curated a comprehensive dataset encompassing 27 distinct cast-forged AZ80 magnesium alloy components, characterized by an extensive range of investigated process parameters, each inducing diverse microstructure features. During the model training phase, several conditions are reserved as test benchmarks to evaluate DDPM's predictive capabilities for unseen scenarios. The microstructure variation in the real image dataset results from applying several different process parameters, such as the pre-forming cast geometry, casting cooling rate, pre-forging heat-treatment, pre-forging soaking process, forging temperature, location of extracted sample, and image magnification. Our previous in-depth studies of this process have shown that in this system a complex relationship exists between process parameters and evolution of the microstructure [45]. The casting cooling rate controls the α -Mg grain size and the morphology of Mg₁₇Al₁₂ phase. During the forging stage, dynamic recrystallization (DRX), which itself depends on initial cast microstructure features like grain size and Mg₁₇Al₁₂ precipitates, introduces a new paradigm in the grain size evolution of the material. The occurrence and grain size of DRX are also affected by forging temperature and the extent of deformation [46]. Also, depending on the initial Mg₁₇Al₁₂ phase in the cast material, dissolution and precipitation of Mg₁₇Al₁₂ particles might occur during the forging process. This complex, but subtle interaction of different microstructure features provides a good testament to DDPMs models' ability of capturing underlying physics in data. To the best of our knowledge, this is the first time that 512×512 pixels images of a wide range of microstructures resulting from several process parameters are synthesized with a deep learning model. We have demonstrated the ability of the proposed model to capture physics information at a level where they can generate images with accurate microstructure features, even for unseen process parameters.

2. Materials and methods

2.1. Manufacturing process

We first cast-forged an AZ80 magnesium alloy to form an SEM microstructure image dataset of 434 grayscale 1024×768-pixel images. The material is cast *via* a permanent mold and die-forged into an asymmetric I-crossbeam geometry (hereafter, referred to as I-beam) in order to resemble the production of complex-shaped structural components [47]. The material is initially cast into either cylindrical billets (diameter 63.5 mm) or a pre-form shape to investigate the effect of the stock geometry in the final properties. The cylinder and pre-form casts are shown in Fig. 1a. With and without using cooling channels and different preheats of 50 °C and 300 °C, three different cooling rates of 10.4, 6 and 1.5 °C/s are achieved for cylinder and pre-form casts. In one scenario, the sample is homogenized after casting process at 420 °C for 24 h. The cylinder billets or pre-form shape components are held for 3 h in the furnace to ensure temperature uniformity (pre-forging soaking). For most samples the pre-forging soaking treatment is conducted at the same temperature as the forging process. Two different scenarios are also applied for the samples forged at 250 °C, in which they are held for 1.5 h or 2 h at 350 °C before being cooled down to the forging temperature for the rest of the soaking time. Forging is performed at isothermal temperatures in a closed-die, restricting material flow in radial and longitudinal directions. The process is carried out in a single step with an initial displacement rate of 6 mm/s using an Interlaken 500-ton press. Three different forging temperatures of 250 °C, 300 °C, and 350 °C are investigated. The schematics of the cylinder and pre-form cast billet forgings are represented in Fig. 1b. The schematic of the final cast-forged I-beam components and their top and front view images are also shown in Fig. 1c and 1d, respectively.

The microstructure samples are extracted from three locations across each I-beam, namely the short and tall flanges and web region. These locations represent different applied effective strain and deformation, which in turn result in different final microstructure. All specimens are cold mounted in epoxy and are ground using 120, 400, 800, and 1000 grit SiC paper and polished with 9, 3, 1, 0.25 μ m diamond paste. The final polishing is performed using a 0.05 μ m colloidal silica solution. After each polishing step, specimens are cleaned in an ultrasonic ethanol bath. Etching is performed using the picric-hydrochloric etchant (100 ml ethanol + 4 g picric acid + 3 ml hydrochloric acid + 10 ml distilled water). The microstructure is studied *via* a ZEISS Ultra Plus field emission scanning electron microscope (FE-SEM).

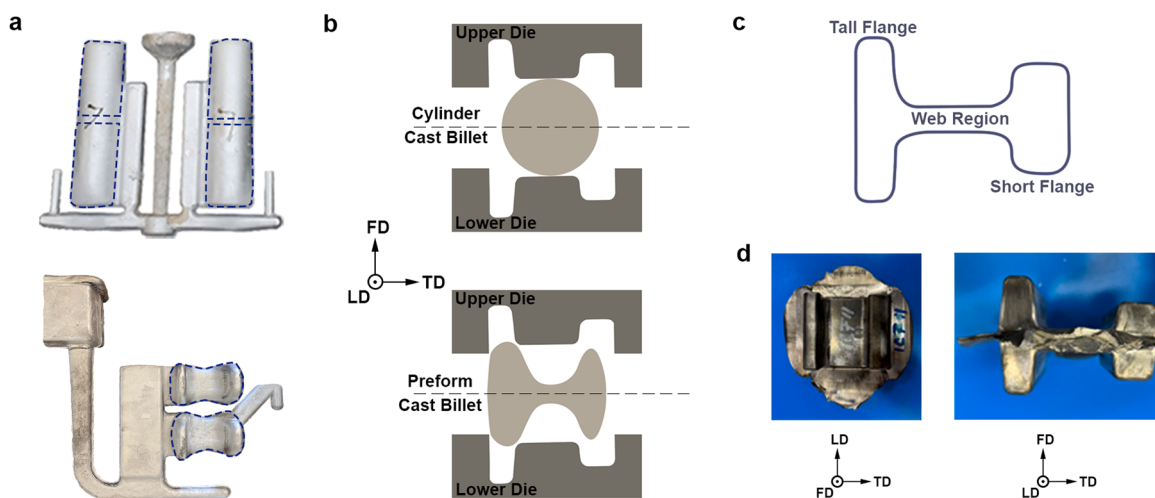


Fig. 1. Manufacturing process of the cast-forged AZ80 I-beams. a, cylinder (top) and pre-form (bottom) casts with the final parts shown with dashed lines. b, schematic of the cylinder (top) and pre-form (bottom) forgings. c, schematic of the final cast-forged I-beam components. d, top (left) and front (right) view images of the cast-forged components before flash trimming.

2.2. Modeling

2.2.1. Data preprocessing

To prepare the training data, the actual 1024×768 images are randomly cropped into 512×512 image size at the beginning of each iteration. Images from 100x, 500x, 1000x, 1500x, 2000x, and 3000x magnifications are selected from different cast-forging processing routes, which ends up in 131 different classes. In order to evaluate the model's predictive ability, we implemented a leave-one-category-out scenarios. In this approach, we set aside 17 image classes during training, which accounts for 13 % of the data. This resulted in test/train split of 13:87 which is different from the more common 20:80 or 10:90 data partitioning. Our focus was on evaluating leave-one-category-out scenarios, and you can find detailed information on this in Section 2.2.4. The model implementation codes are available to download (see Data availability). The training data will be made available upon request. With the available model codes and actual image data, interested readers can retrain the model, selecting the testing/training ratio and classes as they wish. Several transformations are applied to convert the array into a tensor with normalized pixel intensity in the range $[-1,1]$. Since the microstructure images are indifferent to rotation, the data augmentation with the help of random horizontal and vertical flips with a probability of 0.5 is applied to the cropped images.

2.2.2. Denoising diffusion probabilistic model

DDPM models are a class of latent variable models that consist of two processes; a forward process that introduces noise to images, and the backward process which denoises the data. In the forward process, also known as diffusion process, different levels of noise are added to the training images. Using a neural network, the model learns to find the noise distribution added to each training data. This way, the original images can be reconstructed by gradually removing the noise. The aim of this approach process is that the model learns the underlying data distribution; therefore, by applying the trained model to an image sampled from pure noise, the model can denoise it toward generating new images representative of the original dataset. The following is a brief introduction of the model, more details can be found in the original paper [38] and following works [48,49].

During the forward process, the noise is added incrementally in a Markovian process. The forward diffusion kernel, $q(x_t|x_{t-1})$, is a conditional probability which defines the probability distribution of the image at a noisier step, t , given a less noisy state of the image at step $t - 1$. In other words, starting from an image (x_0) sampled from the data distribution $q(x)$, the probability density function of the noisier data, x_t , from its previous step, less noisy x_{t-1} , is computed by Eq. (1), when the noise is sampled from the Normal distribution:

$$q(x_t|x_{t-1}) := \mathcal{N}(x_t; \sqrt{1 - \beta_t}x_{t-1}, \beta_t\mathbf{I}) \quad (1)$$

where, $\beta_t \in (0, 1)$ is the variance schedule (β_t values change over time, e.g., β_1 is small, and β_T is large), and \mathbf{I} is the identity matrix. This allows the posterior, $q(x_{1:T}|x_0)$, to be approximated using a Markov chain,

$$q(x_{1:T}|x_0) := \prod_{t=1}^T q(x_t|x_{t-1}). \text{ By using the notation } \alpha_t := 1 - \beta_t \text{ and } \bar{\alpha}_t := \prod_{s=0}^t \alpha_s, \text{ the noised data at any arbitrary step can be found:}$$

$$q(x_t|x_{t-1}) := \mathcal{N}(x_t; \sqrt{\bar{\alpha}_t}x_0, (1 - \bar{\alpha}_t)\mathbf{I}) \quad (2)$$

With reparameterization, x_t can be written as:

$$x_t = \sqrt{\bar{\alpha}_t}x_0 + \sqrt{1 - \bar{\alpha}_t}\epsilon \quad (3)$$

where, $\epsilon \sim \mathcal{N}(\epsilon|0, \mathbf{I})$.

During the backward process, the goal is to denoise images iteratively to get back to a less noisy version:

$$p(x_{t-1}|x_t) := \mathcal{N}(x_{t-1}; \tilde{\mu}_t(x_t, t), \sigma_t\mathbf{I}) \quad (4)$$

The reverse conditional shown in Eq. (4) does not have a closed form, but the following approximation is derived for that [38]:

$$\tilde{\mu}_t(x_t, t) \approx \frac{1}{\sqrt{\alpha_t}} \left(x_t - \frac{1 - \alpha_t}{\sqrt{1 - \bar{\alpha}_t}} \epsilon_t \right) \quad (5)$$

where, ϵ_t is the noise introduced in step t . The main idea is to learn this distribution, so we can denoise images by the reverse conditional probability. To do this, we train a neural network $\epsilon_\theta(x_t, t)$ to approximate the introduced noise distribution:

$$\text{Minimize } L(\theta) = \|\epsilon_t - \epsilon_\theta(x_t, t)\|_2^2 \quad (6)$$

2.2.3. Model implementation

We implemented the DDPM generative model in Python with the help of Pytorch library. In this work, a U-net architecture, which is first introduced by Ronneberger et al. [50], for image segmentation, is used to find the introduced noise distribution, ϵ_t . Due to its symmetric down-sampling and up-sampling, this architecture is suitable for going from a noisy image to its equivalent denoised version. The encoding part consists of six blocks of max-pooling, each followed by four convolutional layers, group normalization, and Gaussian Error Linear Unit (GELU) activation function. The self-attention mechanism with four heads is applied after each down-sampling layer to help with the long range and multi-level dependencies across image regions [51]. The decoding part is a somewhat mirrored structure of the encoding. It comprises six blocks with bi-linear up-sampling, each followed by four convolutional layers, group normalization, and GELU activation function. The only difference between the decoding and encoding architecture is that after each up-sampling layer the data is concatenated with skip connections corresponding to channels with the same resolution from the encoding part to prevent the loss of spatial information from the encoder layers and mitigate the vanishing gradient problem. The model is conditioned on the time step by the Transformer positional embedding [52], added to each down-sampling and up-sampling layer. To make the model class-conditional, in their original work, Nichol and Dhariwal [49], included class information through the same method as the time step by adding a class embedding to the time step embedding. We found this method ineffective, probably due to the large number of process parameters that are added as different class labels. Instead, in order to condition the model on several specific process parameters, we propose the following approach. At each down-sampling and up-sampling layer, the embedded vectors corresponding to process parameters are linearly mapped into separate tensors with the same size of the corresponding layer spatial dimension and are then concatenated with feature maps of that layer. Adam optimizer and mean squared error (MSE) loss function are used in training of the model. The exponential moving average (EMA) technique that calculates the exponentially weighted average of the current and updated model parameters at each optimization step is used to stabilize the optimization process [49]. The models are trained on the Digital Research Alliance of Canada platform using a P100-16G GPU.

2.2.4. Performance evaluation

The quality of synthesized images is assessed with both IQM and microstructure feature metrics. The FID score is calculated based on the implementation by Seitzer [53]. This metric uses a pre-trained InceptionV3 network [44] to extract features and measures the activation values of intermediate layers to compare the similarity between two image datasets. In this study, the FID score is used to evaluate training convergence and help to avoid overfitting. Although the FID is a very good tool to compare the performance of image generative models by taking into account the image features, it is affected by factors such as the dataset size and image type. In this work, the baseline is the FID

score measured between two subsets of the randomly selected real images. In addition to synthesized vs. real FID score, for comparison, the FID score between a subset of ultra-high carbon steel SEM images taken from [54] and real images is also calculated.

The physics capturing ability of the model is evaluated by analysis of the microstructure features that are shown to affect the material's final mechanical properties [45,47,55]. The percentage of the intermetallic Mg₁₇Al₁₂ compound, the percentage of the DRXed regions, and the DRX grain size are measured for the real and synthesized seen and unseen microstructures. Unseen conditions refer to the process parameter combinations whose SEM images are not used in training of the model, but are used in evaluation of morphological features. Eleven components are cast and forged into an I-beam geometry, and the microstructure samples are extracted from different locations across each I-beam, resulting in 27 metallographic samples. To demonstrate the model performance in predicting the microstructure for unseen processing conditions, which is the main objective of this study, about 13% of the dataset is set aside and not included in the training of the model. These unseen conditions consist of all metallographic samples of one cast-forged I-beam component, one metallographic sample of another cast-forged component, and two magnifications of different metallographic samples, totaling 17 unseen image classes. Due to the substantial computational requirements of the model, we chose not to employ k-fold cross-validation in this work. However, a large number of synthesized images are generated for model evaluation to indicate the model's robustness in microstructure generation. The FID score measurement is conducted between sets of size 200 images, and analysis of the morphological features is calculated using at least 10 images for each condition.

3. Results and discussion

3.1. Synthesized high-resolution images of the cast-forged AZ80 magnesium alloy

The evolution of an example synthesized image from earlier to later training iterations is depicted in Fig. 2. Toward later iterations, the synthesized image develops more features, such as different types of intermetallic morphologies and grain boundary. The FID score for certain iterations is also shown in Fig. 2.

As shown in Fig. 2, the FID score gradually decreases with training for the synthesized vs. real images, indicating more resemblance of the synthesized images with AZ80 microstructure at the end of the training. It is noteworthy that a lower FID score means more similarity, as FID score between two identical datasets is almost zero. Since the study's goal is to produce new variation of images, we established a baseline by comparing two subsets of randomly selected real AZ80 microstructure images. This baseline shows the minimum attainable FID score when various AZ80 images come from the same data distribution.

Also, in order to have a reference for how close the synthesized images are to the real dataset, a comparison with an available real steel SEM dataset, containing microstructure images of pearlite, cementite, martensite, and bainite phases [54], is also provided. In this regard, the FID metric is used to measure the similarity between the real steel microstructure images and our real AZ80 dataset. Although both datasets contain real SEM images, the minimum attainable FID score is significantly higher than the FID score of our synthesized vs. real images. This means that the DDPM model has correctly included image features that are distinguishably representative of an AZ80 magnesium alloy. After 3600 iterations, equivalent of more than 130 h of computation with our available resources, the training is stopped due to no further significant improvement in the FID score.

Fig. 3 shows some examples of the generated images compared to their real counterparts. Based on the real images, it is evident that the different processing routes result in diverse microstructure outcomes,

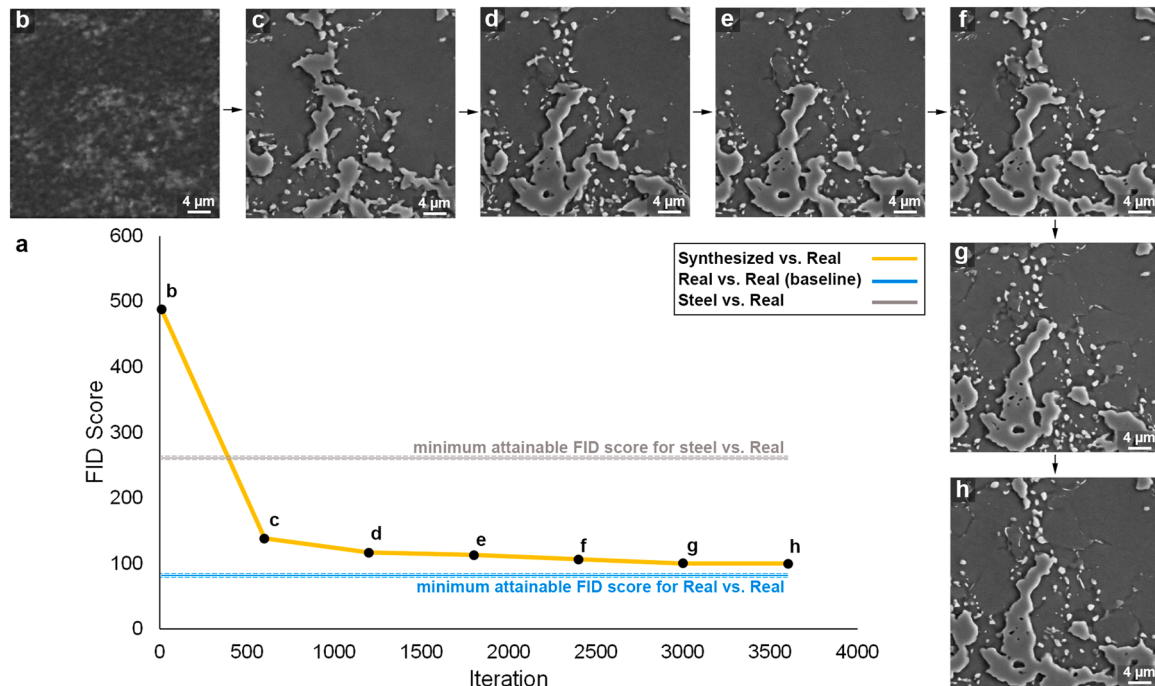


Fig. 2. The model progress with training iterations. a, corresponding FID score of certain iterations of synthesized images vs. real images. The evolution of an example image from the corresponding iteration: b, 30. c, 600. d, 1200. e, 1800. f, 2400. g, 3000. h, 3600 is also shown. Comparisons with FID score of the baseline, calculated from two subsets of the real images, and that of steel SEM images from Ref. [54] vs. the real images are provided. The dotted lines show the standard deviation of the corresponding minimum attainable FID score.

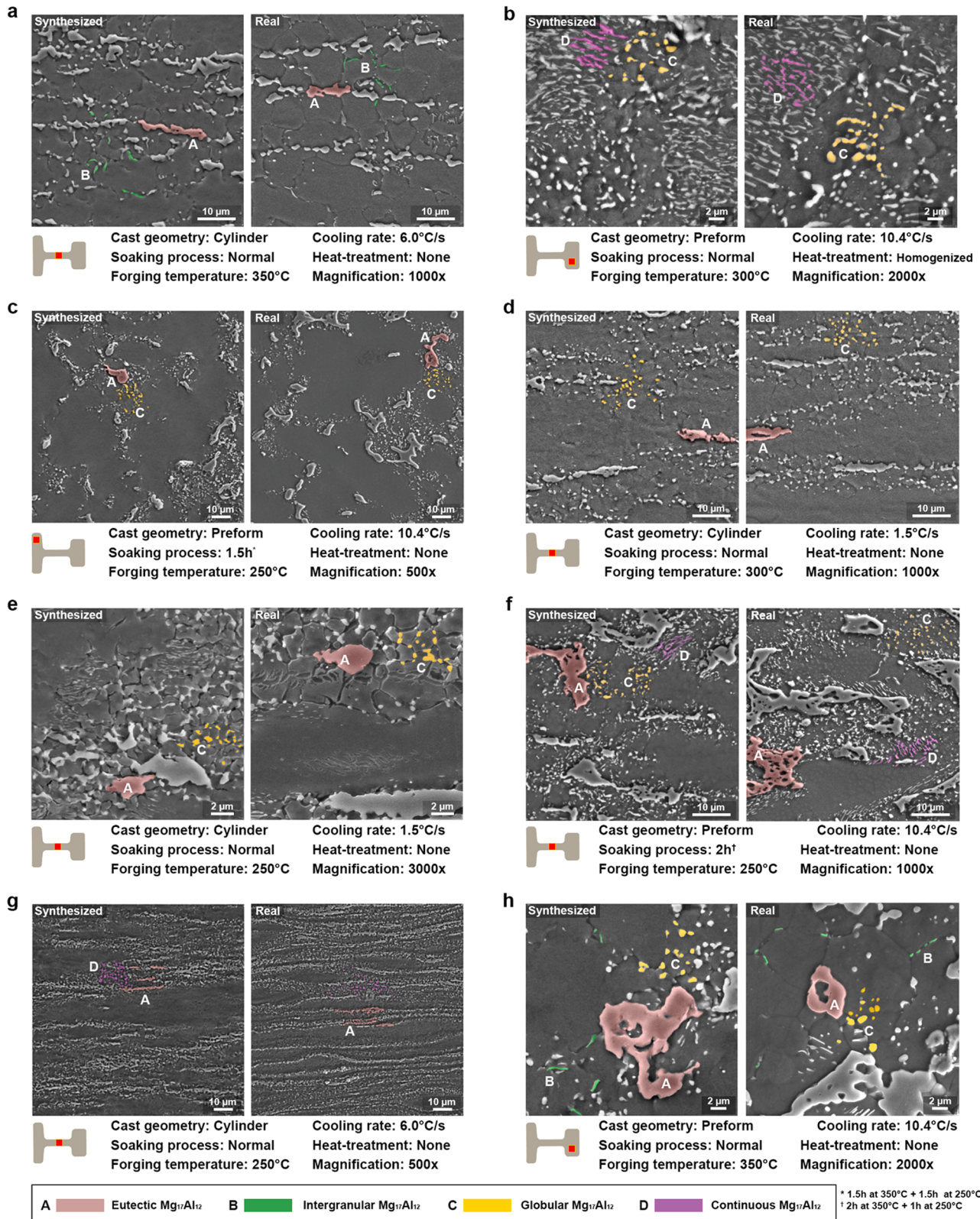


Fig. 3. Pairwise comparison of synthesized and real images for several typical conditions used during training (Seen). The model visually generates images expected by the domain knowledge. a, d, e, f, g: show the microstructure at the web region, undergoing high to severe deformation resulting in breakage and elongation of intermetallic particles. b: showing the microstructure of pre-forging homogenization heat treatment and the ineffectiveness of the continuous morphology in promoting DRX. c: example of components with low deformation, retaining its initial cast structure. It shows the model's ability to capture microstructure heterogeneities. a, d: show the microstructure of components with uniform distribution of $Mg_{17}Al_{12}$ particles, resulting in fully recrystallized regions. e, g: show the effect of $Mg_{17}Al_{12}$ particles on promoting dynamic recrystallization; DRXed grains are prevalent at regions containing the eutectic and discontinuous $Mg_{17}Al_{12}$ morphologies.

yet the images generated by DDPM visually seem to successfully imitate every class. The studied ranges of the casting and forging processes produce different morphologies of the $Mg_{17}Al_{12}$ intermetallic compound. These are eutectic, lamellar, continuous, and globular and intergranular forms of discontinuous $Mg_{17}Al_{12}$ phase. The microstructure resulting from each process conditions is dominated by certain morphologies. These features are highlighted in Fig. 3 demonstrating the model's ability to assign the correct types of $Mg_{17}Al_{12}$ morphologies for different conditions.

At the web region of I-beams, severe deformation results in elongated grain and intermetallic compound particles, this can be seen in Fig. 3a and d–g. The extent of effective strain at the web region is less in samples produced from pre-form cast geometry, and this results in slightly less elongated features (Fig. 3f). The synthesized images show this elongation of grain and $Mg_{17}Al_{12}$ particles; they also represent the difference between cylinder and pre-form cast-forged components.

Our previous microstructure study of interactions between the $Mg_{17}Al_{12}$ intermetallic phase and DRX phenomenon in the AZ80 magnesium alloy has shown that during the forging stage, the occurrence of dynamic recrystallization introduces fine grains into the microstructure. In addition, it is shown that the eutectic, lamellar, and discontinuous globular morphologies of the $Mg_{17}Al_{12}$ phase effectively promote the occurrence of dynamic recrystallization, while the continuous morphology is only effective when the particles are broken as a result of a high amount of deformation. Similarly, the synthesized images show finer grains around the eutectic and discontinuous $Mg_{17}Al_{12}$ particles, not the regions free from them, resulting in a bi-modal, so-called neckless structure (Fig. 3e and g). At the same time, regions with uniform distribution of the intermetallic particles show fully recrystallized regions (Fig. 3a and d), and the continuous $Mg_{17}Al_{12}$ morphology seems not to promote DRX (Fig. 3b), similar to the real images.

The comparison of the synthesized and real images of unseen conditions is shown in Fig. 4 for a few representative conditions. More examples of seen and unseen generated vs. real images is provided in the Supplementary information.

Fig. 4a shows the comparison of the synthesized and real images for the web region and short flange metallography samples of the I-beam component that has been set aside from the training process. Even for this totally unseen condition, the model is able to generate SEM microstructure images that obey domain knowledge expectations. At the short flange, small applied effective strain does not cause severe deformation; therefore, the $Mg_{17}Al_{12}$ eutectic intermetallic retains its characteristic eutectic structure. Comparing the real and synthesized images at 500x magnification indicates that the model clearly yields the same outcome. This completely unseen component is forged at 300 °C. Our microstructure and controlled heat treatment studies have previously shown that without pre-forging homogenization heat treatment, this forging condition results in only the globular $Mg_{17}Al_{12}$ particles in addition to the $Mg_{17}Al_{12}$ eutectic phase. This temperature is above overlapping of discontinuous and continuous morphologies of the $Mg_{17}Al_{12}$ phase, and due to low solubility of Al in Mg at this temperature, $Mg_{17}Al_{12}$ precipitates prior to forging and no intergranular $Mg_{17}Al_{12}$ morphology is formed. As shown in Fig. 4a, the model again correctly captures this physical relationship. Furthermore, the uniform formation of the continuous $Mg_{17}Al_{12}$ phase with globular morphology in between (shown in Fig. 4c-left) and feature size consistency at different magnifications can be mentioned.

3.2. Analysis of the physics information capturing ability

While the visual similarity of the synthesized and real images is obtained as a byproduct of our approach, this has not been the goal of our study. We aimed for the synthesized images to capture microstructure features associated with each certain processing route. In fact, in this study the model is designed to incorporate all the process parameters that previous studies shown to control the microstructure to

establish the process-structure-property relationship of this manufacturing process. Therefore, the implementation of this model is deemed successful only if the model is able to provide images that follow the same trend in physical properties as the real data.

Our previous studies of the AZ80 magnesium alloy have shown the significant effect of the $Mg_{17}Al_{12}$ intermetallic compound and the α -Mg grain size on mechanical properties of the material [55]. Accordingly, we included the most important microstructure features in analysis of physics information capturing ability of the model. Dynamic recrystallization introduces fine grain size that increase the strength and toughness compared to the cast microstructure, and also reduce texture intensification occurred during forging [46,47,56]. The intermetallic $Mg_{17}Al_{12}$ phase affect mechanical properties both directly and indirectly via affecting DRX process. The homogeneity of the microstructure after cast-forging process, that comes from the DRX phenomenon, determines the ductility of the components.

In this regard, the area fraction of the intermetallic $Mg_{17}Al_{12}$ compound, the percentage of the DRXed regions, and the DRX grain size are measured for the real and synthesized seen and unseen microstructures. The results for all 11 cast-forged components are presented in Fig. 5. A complete detail of the metallography samples and their use in training and evaluation is provided in a Supplementary Information document, accessible through the online version of the paper. In all three cases, the properties measured from the synthesized images show the same trend and variation as those measured from the real data. The prediction of microstructure features from the synthesized images results in the percentage of the average errors of $7.06\% \pm 1.27$, $6.46\% \pm 1.61$, and $5.96\% \pm 1.13$ for the percentage of the DRXed regions, the percentage of the intermetallic $Mg_{17}Al_{12}$ compound, and the DRX grain size, respectively. Regarding the predictive capability of the model, the average error of measured properties for seen and unseen conditions are $6.36\% \pm 0.42$ and $6.67\% \pm 0.85$, respectively.

The percentage of DRXed regions is affected by the forging temperature, distribution of the intermetallic $Mg_{17}Al_{12}$ particles, and applied effective strain. At higher temperatures, the effect of forging temperature dominates and results in a fully recrystallized microstructure. At lower forging temperatures, the second phase role via particle stimulated nucleation (PSN) mechanism has comparable effects and results in varied percentage of DRXed regions based on the material history. This factor is measured at the web region of the cast-forged I-beams, and since the components forged from a pre-form shape undergo lower deformation at the web region, they show less recrystallized microstructure. All these aspects are captured by the model generated images.

The percentage of the $Mg_{17}Al_{12}$ intermetallic is measured for all $Mg_{17}Al_{12}$ morphologies. Therefore, its variation with processing parameters is very complicated since it depends on initial cast structure and dissolution and precipitation of different morphologies during the pre-forging and forging stages. Still the model is able to provide an accurate account of this microstructure feature even for prediction of unseen conditions.

The DRX grain size is temperature dependent, and as the forging temperature increases the grain growth results in larger grains. Nevertheless, the DRX grain size variations due to the amount and distribution of second phase particles are captured well by the model. These results unequivocally confirm that DDPM-generated images not only visually resemble real cast-forged AZ80 microstructure but also retain crucial information related to morphological features. This observation substantiates the model's adeptness at capturing the underlying data distribution in a physically meaningful manner.

4. Conclusion

The aim of this study was to investigate the potential of an advanced deep learning structure, called DDPM, in generating high-quality SEM images that include detailed features that are found in real microstructure. In doing so, a DDPM was adopted, trained on the images captured

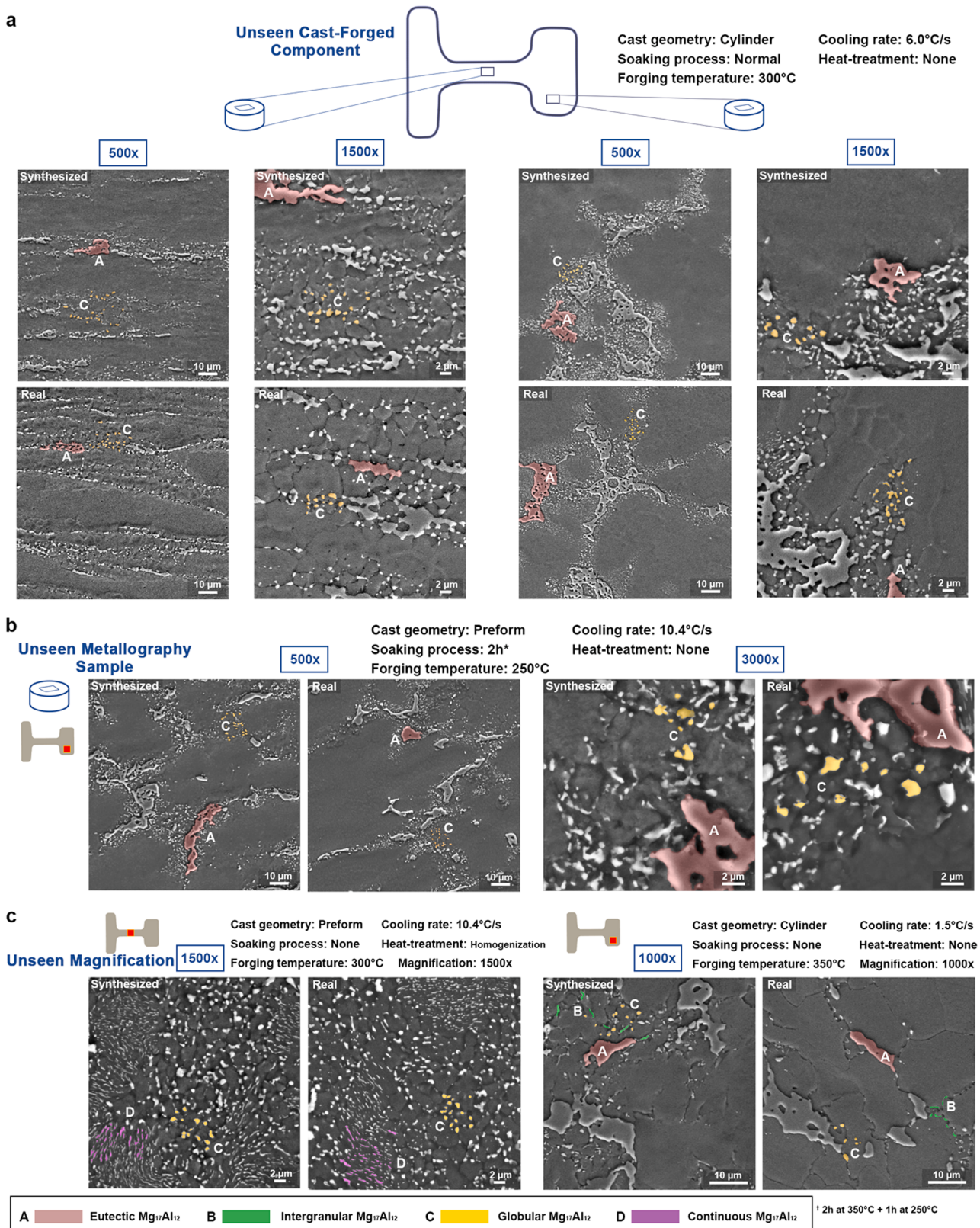


Fig. 4. Pairwise comparison of real and synthesized images for several examples of conditions not used during training (Unseen). Real and synthesized SEM images corresponding to a: one-I-beam-out scenario, in which all images from all locations of a cast-forged component are set aside and not used in the model's training. Due to severe deformation at the web region, the microstructure is more deformed and elongated compared to the short flange. In addition to location differences, the model is also able to correctly generate existing Mg₁₇Al₁₂ morphologies for this processing route. b: one-sample-out scenario, in which all images of one metallography sample of a cast-forged component are set aside and not used during training. It visually shows the model ability to capture morphological feature size depending on the image magnification. c: one-magnification-out scenarios, in which all images of one magnification of a metallography sample are set aside and not used during the training. They show the model's ability to include correct morphological features.

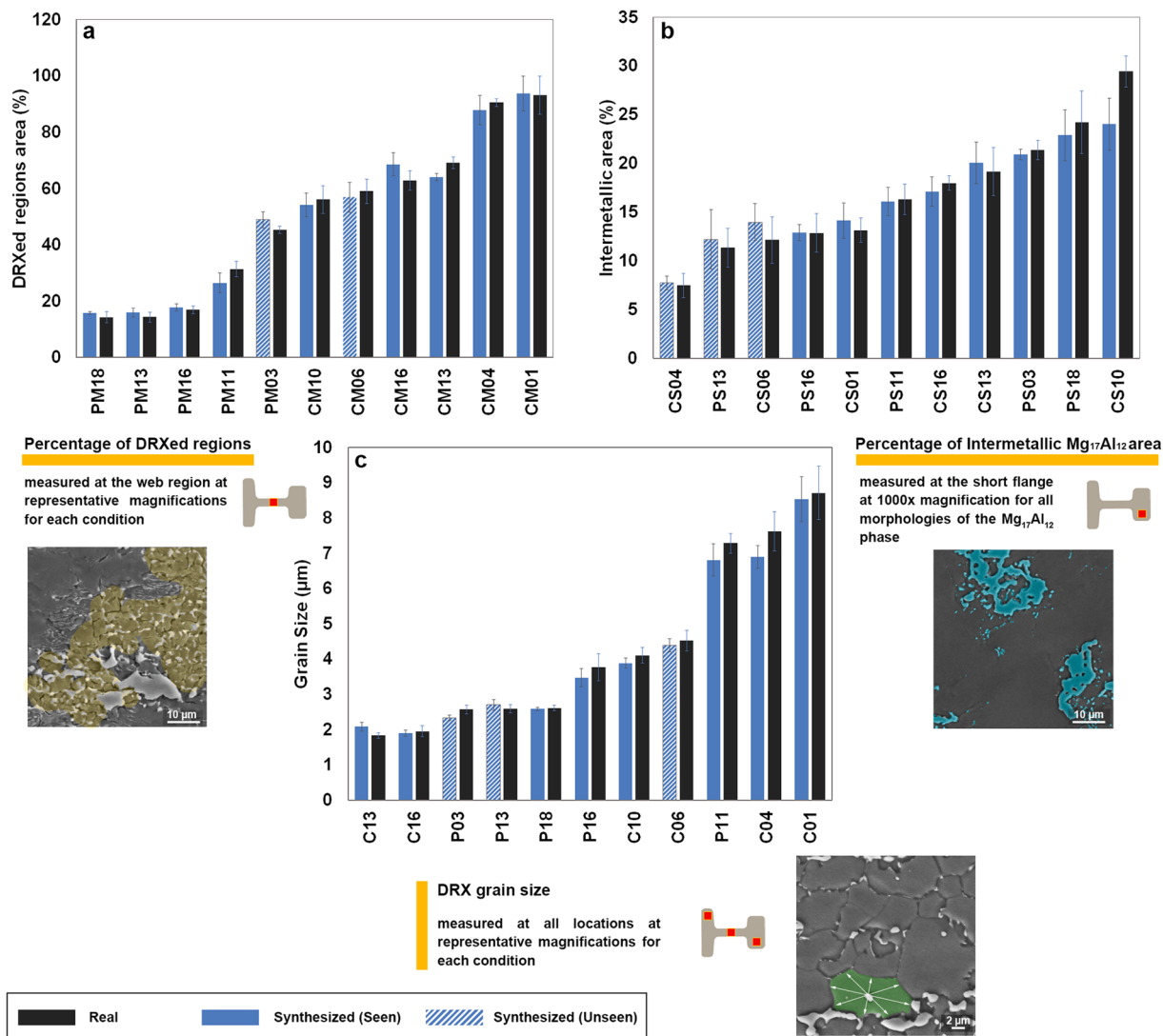


Fig. 5. The morphological properties analysis of the real and synthesized (seen and unseen) images. The comparison of the a, percentage of DRXed regions, measured at the web region of each I-beam at magnifications representative of each condition. b, percentage of total $Mg_{17}Al_{12}$ intermetallic compound phase, measured at the short flange of each I-beam at 1000x magnification. c, DRX grain size, measured at all available locations of each I-beam at magnifications representative of each condition.

from cast-forging of AZ80, and conditioned on the process parameters. In the current study, a complete experimental analysis of the process parameters space would require 108 components to be cast-forged and 324 samples to be extracted for metallography investigation. By analysis of 27 samples (about 8 % of previously required samples) from 11 cast-forged components and applying the presented modeling method, a vast portion, if not all, of the process parameters space can be generated. A detailed investigation on the ability of DDPM in capturing physical relationships between several process parameters and microstructure features was provided demonstrating the success of this approach in predicting the microstructural features of unseen conditions. Based on the results presented, following conclusions can be drawn:

- DDPM model successfully generates high resolution real-looking SEM microstructure images of the cast-forged AZ80 magnesium alloy based on the process parameters inputs, including the pre-forming cast geometry, casting cooling rate, pre-forging heat-treatment, pre-forging soaking process, forging temperature, location of extracted sample, and image magnification.
- The synthesized images resemble the real dataset in regard to microstructure features of the cast-forged AZ80 alloy. The dominant

$Mg_{17}Al_{12}$ intermetallic morphology, extent of deformation, and distribution of dynamically recrystallized regions are correctly captured in the synthesized images for each processing route.

- The comparison of the percentage of the intermetallic $Mg_{17}Al_{12}$ compound, the percentage of the DRXed regions, and the DRX grain size calculated from the synthesized and real images reveal that the synthesized images contain same morphological information as the real dataset. A quantitative comparison of the microstructure features between the synthesized images with the real ones show average differences of $7.06\% \pm 1.27$, $6.46\% \pm 1.612$, and $5.96\% \pm 1.13$ for the percentage of the DRXed regions, the percentage of the intermetallic $Mg_{17}Al_{12}$ compound, and the DRX grain size, respectively.
- The analysis of the model's predictive capability by comparing the morphological features of seen and unseen conditions results in the measured properties average error of $6.36\% \pm 0.42$ and $6.67\% \pm 0.85$ for seen and unseen conditions, respectively, indicating the same level of image similarity and physical relationship capturing ability as the process conditions used during the model training.

The incorporation of advanced ML methods in material science-

related SEM image generation holds immense promise. In this study, we demonstrated that DDPM can produce high-resolution images that capture the physical relationships between process parameters and microstructure features, even for unseen conditions. The model's success in generating images with morphological information similar to real ones opens up possibilities for efficient material design and manufacturing. By analyzing a subset of samples, we could generate a significant portion of the process parameters space, saving time and costs. Furthermore, with its ability to capture physics information, this model has potential as an intermediate step to predict mechanical properties of unseen conditions. Beyond its practical applications, this model can also serve as a virtual microscope and an educational tool, offering diverse microstructure variations at different magnifications.

Data availability

The model implementation codes can be download from <https://github.com/PMysticism/AZ80-DDPM>. Additionally, an image generation module along with the trained model parameters, is available at <https://www.kaggle.com/code/erfanaz/az80-image-generation>. You need to sign in into your Kaggle account or register for one to access this module. This module allows users to use the trained DDPM model and generate cast-forged AZ80 magnesium SEM images by selecting desired process parameters. The instruction for using this module is provided via the link.

The real image dataset used for training and evaluation of the model is available from the corresponding author upon request.

Declaration of Competing Interest

The authors declare that they have no known competing financial interests or personal relationships that could have appeared to influence the work reported in this paper.

Acknowledgment

The authors would like to acknowledge the financial contribution from the Natural Sciences and Engineering Research Council of Canada (NSERC), through their Strategic Partnership Grant STPGP 521551. The authors would also like to thank CanmetMATERIALS, Hamilton, Ontario for performing the casting and forging of the samples at their facilities. This research was enabled in part by support provided by the Digital Research Alliance of Canada (alliancecan.ca).

Supplementary materials

Supplementary material associated with this article can be found, in the online version, at [doi:10.1016/j.actamat.2023.119406](https://doi.org/10.1016/j.actamat.2023.119406).

References

- [1] J. Sohl-Dickstein, E.A. Weiss, N. Maheswaranathan, S. Ganguli, Deep unsupervised learning using nonequilibrium thermodynamics, in: Proceedings of the International Conference on Machine Learning 37, 2015, pp. 2256–2265.
- [2] A. Ramesh, P. Dhariwal, A. Nichol, C. Chu, M. Chen, Hierarchical text-conditional image generation with clip latents, ArXivabs/2204.06125 (2022), <https://doi.org/10.48550/arXiv.2204.06125>.
- [3] P. Acar, Machine learning approach for identification of microstructure–process linkages, AIAA J. 57 (8) (2019) 3608–3614, <https://doi.org/10.2514/1.J058244>.
- [4] Y. Liu, S.J. Chen, K. Sagoe-Crentsil, W. Duan, Large set microstructure reconstruction mimicking quantum computing approach via deep learning, Acta Mater. 230 (2022), 117860, <https://doi.org/10.1016/j.actamat.2022.117860>.
- [5] H.K.D.H. Bhadeshia, Neural networks in materials science, ISIJ Int. 39 (1999) 966–979.
- [6] Y. Liu, T. Zhao, W. Ju, S. Shi, Materials discovery and design using machine learning, J. Mater. 3 (3) (2017) 159–177, <https://doi.org/10.1016/j.jmat.2017.08.002>.
- [7] B.L. DeCost, T. Francis, E.A. Holm, Exploring the microstructure manifold: image texture representations applied to ultrahigh carbon steel microstructures, Acta Mater. 133 (2017) 30–40, <https://doi.org/10.1016/j.actamat.2017.05.014>.
- [8] D.A. Cogswell, W.C. Carter, Thermodynamic phase-field model for microstructure with multiple components and phases: the possibility of metastable phases, Phys. Rev. E 83 (6) (2011), 061602, <https://doi.org/10.1103/PhysRevE.83.061602>.
- [9] S. Florez, M. Shakoor, T. Toulonge, M. Bernacki, A new finite element strategy to simulate microstructural evolutions, Comput. Mater. Sci. 172 (2020), 109335, <https://doi.org/10.1016/j.commatsci.2019.109335>.
- [10] D. Tourret, H. Liu, J. Llorca, Phase-field modeling of microstructure evolution: recent applications, perspectives and challenges, Prog. Mater. Sci. 123 (2022), 100810, <https://doi.org/10.1016/j.pmatsci.2021.100810>.
- [11] Y. Chen, C.A. Schuh, A coupled kinetic Monte Carlo–finite element mesoscale model for thermoelastic martensitic phase transformations in shape memory alloys, Acta Mater. 83 (2015) 431–447, <https://doi.org/10.1016/j.actamat.2014.10.011>.
- [12] S. Suresh, S.-W. Lee, M. Aindow, H.D. Brody, V.K. Champagne Jr, A.M. Dongare, Unraveling the mesoscale evolution of microstructure during supersonic impact of aluminum powder particles, Sci. Rep. 8 (2018) 10075, <https://doi.org/10.1038/s41598-018-28437-3>.
- [13] S. Chun, S. Roy, Y.T. Nguyen, J.B. Choi, H.S. Udaykumar, S.S. Baek, Deep learning for synthetic microstructure generation in a materials-by-design framework for heterogeneous energetic materials, Sci. Rep. 10 (2020) 13307, <https://doi.org/10.1038/s41598-020-70149-0>.
- [14] C. Fragassa, M. Babic, C.P. Bergmann, G. Minak, Predicting the tensile behaviour of cast alloys by a pattern recognition analysis on experimental data, Metals 9 (5) (2019) 557, <https://doi.org/10.3390/met9050557> (Basel).
- [15] Z.-L. Wang, Y. Adachi, Property prediction and properties-to-microstructure inverse analysis of steels by a machine-learning approach, Mater. Sci. Eng. A 744 (2019) 661–670, <https://doi.org/10.1016/j.msea.2018.12.049>.
- [16] J. Feng, Q. Teng, X. He, X. Wu, Accelerating multi-point statistics reconstruction method for porous media via deep learning, Acta Mater. 159 (2018) 296–308, <https://doi.org/10.1016/j.actamat.2018.08.026>.
- [17] V. Oommen, K. Shukla, S. Goswami, R. Dingreville, G.E.M. Karniadakis, Learning two-phase microstructure evolution using neural operators and autoencoder architectures, NPJ Comput. Mater. 8 (2022) 190, <https://doi.org/10.1038/s41524-022-00876-7>.
- [18] R. Kondo, S. Yamakawa, Y. Masuoka, S. Tajima, R. Asahi, Microstructure recognition using convolutional neural networks for prediction of ionic conductivity in ceramics, Acta Mater. 141 (2017) 29–38, <https://doi.org/10.1016/j.actamat.2017.09.004>.
- [19] S.M. Azimi, D. Britz, M. Engstler, M. Fritz, F. Mücklich, Advanced steel microstructural classification by deep learning methods, Sci. Rep. 8 (2018) 2128, <https://doi.org/10.1038/s41598-018-20037-5>.
- [20] D. Ciregan, U. Meier, J. Schmidhuber, Multi-column deep neural networks for image classification, in: Proceedings of the IEEE Conference on Computer Vision and Pattern Recognition, 2012, pp. 3642–3649, <https://doi.org/10.1109/CVPR.2012.6248110>.
- [21] K. Haan, Z.S. Ballard, Y. Rivenson, Y. Wu, A. Ozcan, Resolution enhancement in scanning electron microscopy using deep learning, Sci. Rep. 9 (2019) 12050, <https://doi.org/10.1038/s41598-019-48444-2>.
- [22] Y. Rivenson, Z. Göröcs, H. Güneydin, Y. Zhang, H. Wang, A. Ozcan, Deep learning microscopy, Optica 4 (2017) 1437–1443.
- [23] A. Iyer, B. Dey, A. Dasgupta, W. Chen, A. Chakraborty, A conditional generative model for predicting material microstructures from processing methods, ArXivabs/1910.02133 (2019), <https://doi.org/10.48550/arXiv.1910.02133>.
- [24] T. Hsu, W.K. Epting, H. Kim, H.W. Abernathy, G.A. Hackett, A.D. Rollett, P. A. Salvador, E.A. Holm, Microstructure generation via generative adversarial network for heterogeneous, topologically complex 3D materials, JOM 73 (2021) 90–102, <https://doi.org/10.1007/s11837-020-04484-y>.
- [25] Y. Kim, H.K. Park, J. Jung, P. Asghari-Rad, S. Lee, J.Y. Kim, H.G. Jung, H.S. Kim, Exploration of optimal microstructure and mechanical properties in continuous microstructure space using a variational autoencoder, Mater. Des. 202 (2021), 109544, <https://doi.org/10.1016/j.matdes.2021.109544>.
- [26] K.-H. Lee, G.J. Yun, Microstructure reconstruction using diffusion-based generative models, Mech. Adv. Mater. Struct. (2023) 1–19, <https://doi.org/10.1080/15376494.2023.2198528>.
- [27] C. Düreth, P. Seibert, D. Rücke, S. Handford, M. Kästner, M. Gude, Conditional diffusion-based microstructure reconstruction, Mater. Today Commun. 35 (2023), 105608, <https://doi.org/10.1016/j.mtcomm.2023.105608>.
- [28] P.C.H. Nguyen, N.N. Vlassis, B. Bahmani, W.C. Sun, H.S. Udaykumar, S.S. Baek, Synthesizing controlled microstructures of porous media using generative adversarial networks and reinforcement learning, Sci. Rep. 12 (2022) 9043, <https://doi.org/10.1038/s41598-022-12845-7>.
- [29] J. Lee, N.H. Goo, W.B. Park, M. Pyo, K. Sohn, Virtual microstructure design for steels using generative adversarial networks, Eng. Rep. 3 (2021) 1–14, <https://doi.org/10.1002/eng2.12274>.
- [30] M. Arjovsky, S. Chintala, L. Bottou, "Wasserstein GAN," arXiv preprint, p. arXiv: 1701.07875; 10.48550/arXiv.1701.07875., 2017.
- [31] I. Gulrajani, F. Ahmed, M. Arjovsky, V. Dumoulin, A. Courville, Improved training of Wasserstein Gans, Proceedings of the Advances in Neural Information Processing Systems (2017) 5767–5777, <https://doi.org/10.48550/arXiv.1704.00028>.
- [32] H. Thanh-Tung, T. Tran, Catastrophic forgetting and mode collapse in GANs, in: Proceedings of the 2020 International Joint Conference on Neural Networks (IJCNN), 2020, pp. 1–10, <https://doi.org/10.1109/IJCNN48605.2020.9207181>.
- [33] R. Shams, M. Masih, R.B. Boozarjomehry, M.J. Blunt, A hybrid of statistical and conditional generative adversarial neural network approaches for reconstruction of 3D porous media (ST-CGAN), Adv. Water Resour. 158 (2021), 104064, <https://doi.org/10.1016/j.advwatres.2021.104064>.

- [34] R. Durall, A. Chatzimichailidis, P. Labus, J. Keuper, Combating mode collapse in GAN training: an empirical analysis using Hessian Eigenvalues, in: Proceedings of the 16th International Joint Conference on Computer Vision, Imaging and Computer Graphics Theory and Applications, 2020, <https://doi.org/10.48550/arXiv.2012.09673>. Volume 4.
- [35] A. Plumerault, H. Borgne, C. Hudelot, AVAE: adversarial variational auto encoder, in: Proceedings of the 2020 25th International Conference on Pattern Recognition (ICPR), 2020, <https://doi.org/10.1109/ICPR48806.2021.9412727>. Corpus ID: 229339786.
- [36] S. Zhao, J. Song, S. Ermon, Towards deeper understanding of variational autoencoding models, ArXiv abs/1702.08658 (2017), <https://doi.org/10.48550/arXiv.1702.08658>.
- [37] S. Thakre, V. Karan, A.K. Kanjarla, Quantification of similarity and physical awareness of microstructures generated via generative models, Comput. Mater. Sci. 221 (2023), 112074, <https://doi.org/10.1016/j.commatsci.2023.112074>.
- [38] J. Ho, A. Jain, P. Abbeel, Denoising diffusion probabilistic models, Adv. Neural Inf. Process Syst. 33 (2020) 6840–6851, <https://doi.org/10.48550/arXiv.2006.11239>.
- [39] N.N. Vlassis, W.C. Sun, Denoising diffusion algorithm for inverse design of microstructures with fine-tuned nonlinear material properties, ArXivabs/2302.12881 (2023), <https://doi.org/10.48550/arXiv.2302.12881>.
- [40] E. Lejeune, Mechanical MNIST: a benchmark dataset for mechanical metamodels, Extreme Mech. Lett. 36 (2020), 100659, <https://doi.org/10.1016/j.eml.2020.100659>.
- [41] S. Kastrulyin, J. Zakirov, D. Prokopenko, D.V. Dylov, PyTorch image quality: metrics for image quality assessment, ArXivabs/2208.14818 (2022), <https://doi.org/10.48550/arXiv.2208.14818>.
- [42] R. Kazmierczak, G. Franchi, N. Belkhir, A. Manzanera, D. Filliat, A study of deep perceptual metrics for image quality assessment, ArXivabs/2208.14818 (2022), <https://doi.org/10.48550/arXiv.2202.08692>.
- [43] M. Heusel, H. Ramsauer, T. Unterthiner, B. Nessler, S. Hochreiter, GANs trained by a two time-scale update rule converge to a local Nash equilibrium, Adv. Neural Inf. Process Syst. 30 (2017) 6626–6637.
- [44] C. Szegedy, V. Vanhoucke, S. Ioffe, J. Shlens, Z. Wojna, Rethinking the inception architecture for computer vision, in: Proceedings of the IEEE Conference on Computer Vision and Pattern Recognition, 2016, pp. 2818–2826, <https://doi.org/10.48550/arXiv.1512.00567>.
- [45] E. Azqadan, J. Uramowski, A.A. Roostaei, S.B. Behravesh, A. Javaid, B. W. Williams, M.A. Wells, H. Jahed, The effect of cooling rate and degassing on microstructure and mechanical properties of cast AZ80 magnesium alloy, Mater. Sci. Eng. A 844 (2022), 143176, <https://doi.org/10.1016/j.msea.2022.143176>.
- [46] P. Prakash, D. Toscano, S.K. Shah, M.A. Wells, H. Jahed, B.W. Williams, Effect of temperature on the hot deformation behavior of AZ80 magnesium alloy, Mater. Sci. Eng. A 794 (2020), 139923.
- [47] A. Gryguc, S.B. Behravesh, S.K. Shah, H. Jahed, M. Wells, B. Williams, X. Su, Low-cycle fatigue characterization and texture induced ratcheting behaviour of forged AZ80 Mg alloys, Int. J. Fatigue 116 (2018) 429–438, <https://doi.org/10.1016/j.ijfatigue.2018.06.028>.
- [48] H. Cao, C. Tan, Z. Gao, G. Chen, P.-A. Heng, SZ. Li, A survey on generative diffusion model, ArXivabs/2209.02646 (2022), <https://doi.org/10.48550/arXiv.2209.02646>.
- [49] A.Q. Nichol, P. Dhariwal, Improved denoising diffusion probabilistic models, in: Proceedings of the International Conference on Machine Learning, 2021, pp. 8162–8171, <https://doi.org/10.48550/arXiv.2102.09672>.
- [50] O. Ronneberger, P. Fischer, T. Brox, U-Net: convolutional networks for biomedical image segmentation, in: Proceedings of the 18th International Conference Medical Image Computing and Computer-Assisted Intervention—MICCAI 2015, Munich, Germany, 2015, pp. 234–241. October 5–9, 2015, Proceedings, Part III 18.
- [51] H. Zhang, I. Goodfellow, D. Metaxas, A. Odena, Self-attention generative adversarial networks, in: Proceedings of the 36th International Conference on Machine Learning, PMLR, 2019, pp. 7354–7363, <https://doi.org/10.48550/arXiv.1805.08318>, 97.
- [52] A. Vaswani, N. Shazeer, N. Parmar, J. Uszkoreit, L. Jones, AN. Gomez, L. Kaiser, I. Polosukhin, Attention is all you need, Adv. Neural Inf. Process Syst. (2017) 5998–6008.
- [53] M. Seitzer, "pytorch-fid: FID score for PyTorch," GitHub Version 0.2: <https://github.com/mseitzer/pytorch-fid>, 2020.
- [54] B.L. DeCost, M.D. Hecht, T. Francis, B.A. Webler, Y.N. Picard, E.A. Holm, UHCSDB: ultraHigh carbon steel micrograph database, Integr. Mater. Manuf. Innov. 6 (2017) 197–205, <https://doi.org/10.1007/s40192-017-0097-0>.
- [55] E. Azqadan, J. Uramowski, M.A. Wells, A. Arami, H. Jahed, Hardness variation in cast-forging process of AZ80 magnesium alloys and its data-driven prediction, Mater. Today Commun. 36 (2023), 106833.
- [56] S.R. Agnew, P. Mehrotra, T.M. Lillo, G.M. Stoica, P.K. Liaw, Texture evolution of five wrought magnesium alloys during route A equal channel angular extrusion: experiments and simulations, Acta Mater. 53 (11) (2005) 3135–3146, <https://doi.org/10.1016/j.actamat.2005.02.019>.